Parabolic Dish Solar Cooker: An Alternative Design Approach Toward Achieving High-Grade Thermal Energy Storage Solution

Sairaj Gaunekar, Amit Shrivastava, and Prodyut Ranjan Chakraborty

1 Introduction

Thermal energy demands associated with cooking is majorly catered by fossil fuels. The ever-increasing global demand for energy over the last century led to extensive usage of fossil fuels, causing the depletion of natural reserves at an alarming rate. It is not only the severe depletion of these natural reserves, but also the adverse effects on the environment due to the burning of fossil fuels, that led the scientific community to explore alternative renewable resources of energy with lesser environmental impact. Solar energy has a tremendous potential to substitute fossil fuels for many energy extensive applications, particularly in those areas having an abundance of solar irradiation. According to NREL (https://www.nrel.gov/gis/data_solar.html), the average Direct Normal Irradiance (DNI) at Jodhpur India is significantly high (~5 $kWh/m^2/day$). The abundance of solar irradiation in and around Jodhpur (aptly named as Sun-city) along with the entire northwestern belt of India (consisting of Rajasthan, Gujrat, Haryana Punjab and part of Madhya Pradesh) makes this region ideal for harvesting solar energy as a renewable alternative. Among various solar photovoltaic and solar thermal applications, the usage of solar thermal energy for household and commercial cooking has a huge potential to replace conventional fossil fuels to a large extent. Barring the monsoon season and few odd cloudy days over the year solar cooking can reliably cater to energy requirement for cooking with zero carbon footprint. However, to make this application acceptable and more appealing at large, we need to improve the technology in terms of flexibility in cooking schedule. Almost all the commercially available solar cookers do not offer this flexibility of cooking schedule. And the handful of those offer this flexibility are based on sensible

S. Gaunekar · A. Shrivastava · P. R. Chakraborty (✉)
Department of Mechanical Engineering, Indian Institute of Technology Jodhpur, Jodhpur 342037, India
e-mail: pchakraborty@iitj.ac.in

H. Tyagi et al. (eds.), *New Research Directions in Solar Energy Technologies*,
Energy, Environment, and Sustainability,
https://doi.org/10.1007/978-981-16-0594-9_12

heat storage with limited storage capacity at comparatively low temperature (~100 to 150 °C) (Cuce 2018). The energy storage density being small for sensible heat storage, large volume of the storage unit poses a big challenge. Large temperature gradient within the storage medium also hinders the optimal utilization of stored heat. Since the energy storage density of latent heat storage is significantly larger than sensible heat storage, the volume of the storage unit can be reduced to a large extent. Latent heat storage mechanism also ensures heat supply during cooking to be maintained within a narrow temperature range. All these special features associated with latent heat thermal energy storage (LHTES) makes this technology an ideal thermal storage solution for providing the flexibility of cooking schedule with concentrated solar cooker.

The latent thermal energy storage unit consists of a metallic storage container filled with PCM. Different ways of cooking require heat supply at different ranges of temperatures, namely boiling (100–150 °C), simmering (120–200 °C), frying (180–250 °C), grilling (200–300 °C), and so on. Therefore, an ideal PCM for the LHTES should have melting temperature above 250 °C to cater to all these cooking requirements. Conclusive details on various types of PCMs along with their thermophysical properties are summarized by Sharma et al. (2009), Zalba et al. (2003), Iverson et al. (2012), and Kenisarin (2010). From these data on thermophysical properties, it is evident that suitable PCMs having melting temperatures in the range of 250–300 °C are mostly pure inorganic salts or salt compositions with thermal conductivity raging between 0.25 and 0.5 W/mK. Therefore, thermal conductivity enhancement of the PCM is one of the key challenges in designing the LHTS for solar cooking. The charging process of the LHTES involves complete melting of the PCM inside the storage container during the on-sun period, thus storing the thermal energy in the form of latent heat slightly above the melting temperature of the PCM. On the other hand, discharging process involves heat release from the storage device during off-sun hours cooking activities, rendering the PCM to resolidify in the process. For the current analysis, the sizing of the LHTES unit is done on the basis of thermal energy requirement for cooking a typical evening meal for a six-member family, with the menu consisting of roti, dal, rice, and vegetables. The major design challenge is storing sufficient energy above 300 °C within on-sun duration (between 10:00 am and 4:00 pm) to meet the abovementioned cooking requirement.

A brief overview on existing literature reporting the usage of latent heat storage unit integrated with solar cookers is now presented. Domanski et al. (1995) presented a box-type solar cooker with concentric cylindrical vessels having the annulus portion filled with magnesium nitrate hexahydrate as the PCM. The experiments revealed that the effectiveness of this box-type solar cooker strongly depends on solar intensity, cooker medium mass, and the thermophysical properties of the PCM. The heat transfer from the PCM to the cooking pot is also observed to be slow during discharging process. Buddhi and Sahoo (1997) also reported the performance of a box-type solar cooker with stearic acid as the latent heat storage medium. One of the major outcomes of their experimental observation is the possibility of cooking two batches of about 200 gm rice per pot per day. The maximum temperature obtained in this setup was around 100–110 °C. Buddhi et al. (2003) presented a box-type

solar cooker with acetanilide as a latent heat storage medium. They used ternary reflectors to increase the solar radiation. Vigneswaran et al. (2017) studied a box-type solar cooker with multiple reflectors where oxalic acid dihydrate is used as the latent heat storage medium. It was observed that time duration to reach melting temperature is reduced when multiple reflector boosters are used. Sharma et al. (2005) experimentally investigated an evacuated tube solar collector coupled with a latent heat storage unit. Commercial-grade erythritol was used as the PCM. Experimental results showed that the system can cook successfully twice, afternoon and evening daily. Temperatures reached more than 110 °C during evening cooking. Hussein et al. (2008) constructed a solar cooker with heat pipes and double flat plate reflectors. It was noted that the ratio of steel wool incorporated with the PCM can be increased to enhance its effective thermal conductivity. Coccia et al. (2018) constructed a double-walled container storage composed of two stainless steel cylindrical pots constructed concentrically. The annular area in between the pots was filled with a PCM consisting of a ternary mixture of nitrite and nitrate salts (53 wt% KNO_3, 40 wt% $NaNO_2$, 7 wt% $NaNO_3$). A significant improvement of load thermal stabilization during the off-sun period is reported when PCM is used as the storage medium. Lecuona et al. (2013) used a parabolic reflector integrated with LHTES having Paraffin and erythritol as PCM. It was reported that it is feasible to cook the three meals for a family during summer and also in winter. Paraffin was recommended to be a better option than erythritol. Kumaresan et al. (2015, 2016) studied a parabolic trough reflector focussing solar radiation onto the absorber tube. Therminol 55 was used as the heat transfer fluid (HTF) and encapsulated of D-mannitol was used as the PCM. It was observed that the tava cooking unit developed could cater heat comparable to an LPG stove running in the simmering mode. Veremachi et al. (2016) designed and developed a double reflector with axis tracking mechanism. A mixture of sodium nitrate and potassium nitrate at a ratio of 60:40 (mol%) was used as the PCM. A hotspot temperature of 277 °C could be attained with moderate temperatures gradient within the storage unit. Bhave and Thakare (2018) proposed a parabolic solar concentrator integrated with LHTES having magnesium nitrate hexahydrate as the storage medium and thermic mineral oil as HTF. It was reported that in about 50 min the PCM temperature reached 135 °C. Fifty grams of rice with 100 ml water were found to be completely cooked in about 30 min. El-Sebaii et al. (2009) studied degradation associated with thermal cycling of commercial-grade acetanilide and magnesium chloride hexahydrate for solar cooker application. Acetanilide was found to be a more promising PCM for this application. Magnesium chloride hexahydrate degrades easily during thermal cycling because of the phase segregation. Foong et al. (2010) performed numerical and experimental study on KNO_3-$NaNO_3$ salt composition (60:40 weight ratio) as the latent heat storage medium. A double reflector-based parabolic dish concentrator is used for this purpose. The storage container is augmented with fins for improving the thermal performance of the storage unit. The temperature range of 227–327 °C was achieved.

The review of the existing literature on solar cookers with integrated LHTES provides a basis for categorizing such solar cookers containing various design aspects with specific salient features. The block diagram presented in Fig. 1 provides a

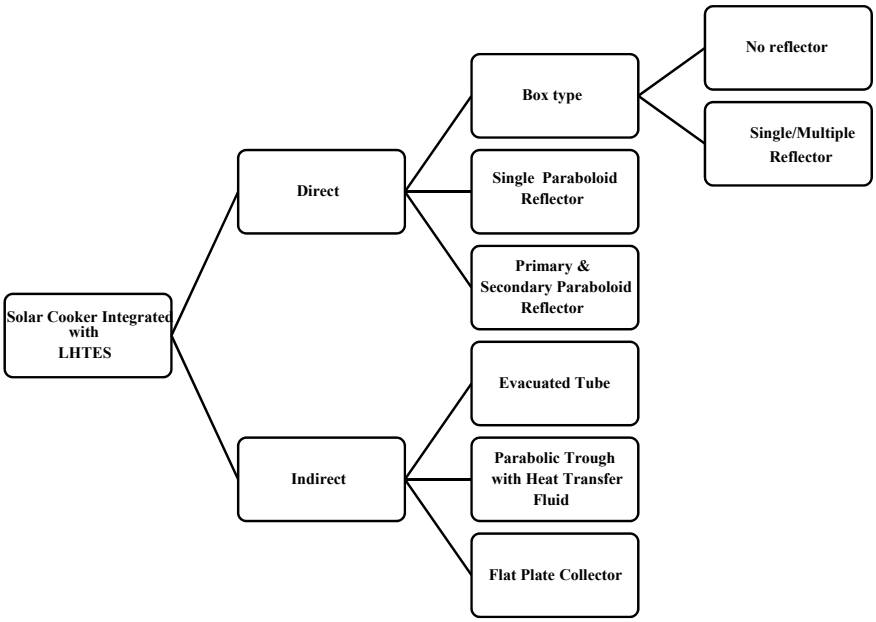

Fig. 1 Classifications of solar cookers with LHTES

consolidated list of existing solar cooker technologies addressing thermal energy storage. The salient features of each of these solar cookers are now discussed in brief.

For direct solar cookers, incident solar radiation is directly used for cooking or storing thermal energy to be dispatched during the hour of need. Solar cookers enlisted in this category are box-type solar cooker, and solar cookers with single or double paraboloid concentrators. Box-type solar cookers can be farther classified as box-cookers without reflector and box-cookers with single or multiple reflectors.

Box-cookers without reflector: Fig. 2 shows a typical design of box-cooker without reflector (Buddhi and Sahoo 1997). A double-walled tray-type container with PCM filled within the space between the walls attributes to the key design feature. The thermal storage tray containing PCM is kept under a glass lid. The upper surface of the tray is covered with absorber material. Sunrays pass through the glass lid, strike the absorber tray, and transfer heat to the PCM underneath it for charging. The tray is surrounded by insulating material. The performance of this type of cooker depends upon the ability of the transparent glass to permit passage of shorter wavelength which forms a significant part of the solar spectrum but opaque to higher wavelength coming out from the box. The temperature inside the box rises because of the green-house effect. However, this setup is found to be inefficient because solar rays are not concentrated by any means, and the charging time is very long.

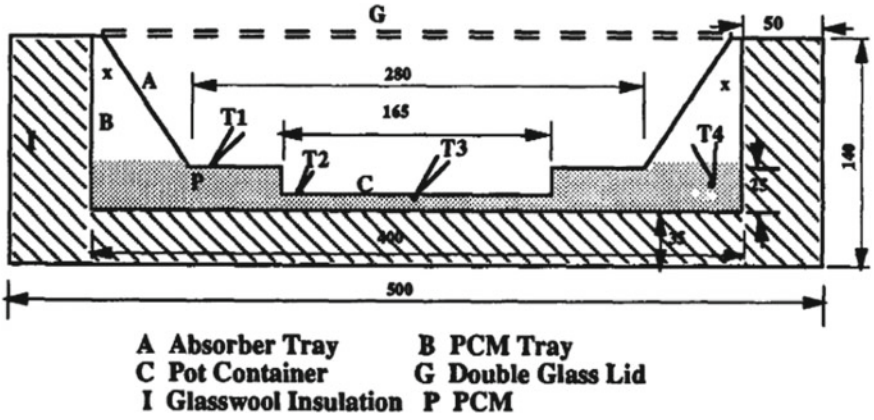

Fig. 2 Schematic of box-cooker without reflector having LHTES (Buddhi and Sahoo 1997)

Box-cookers with single/multiple reflectors: These box-cookers contain single/multiple reflectors (Fig. 3) to concentrate solar radiation on a vessel containing PCM (Vigneswaran et al. 2017). Cooking containers and interior of these box-cookers are made of absorbing material. The box is insulated from sides. The mirrors need to be adjusted with respect to each other to concentrate the solar radiation. Multiple reflectors provide concentrated solar energy to the cooking and storage container enabling the system to achieve temperatures in the range of 100–120 °C.

Concentrated solar cooker with single paraboloid reflector: These solar cookers contain a single paraboloid reflector to concentrate solar irradiation (Fig. 4) on a double-walled container cum cooking pot with PCM filled within the space between the walls Lecuona et al. (2013). The bottom surface of the storage cum cooking container is placed closed to the focal point of the paraboloid reflector. One of the major challenges for this design is associated with continuous solar tracking

Fig. 3 Box-cooker with multiple reflector (Vigneswaran et al. 2017)

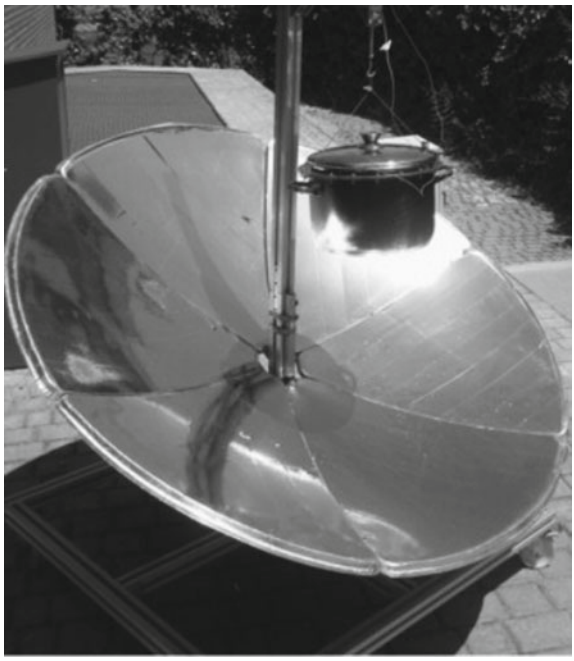

Fig. 4 Solar cooker with paraboloid reflector (Lecuona et al. 2013)

during the operation. Hence, integration of an axis tracking mechanism is a must for this design concept. Locating the heavy storage cum cooking container above the reflector renders this tracking even more challenging. However, we can obtain very high temperatures of about 250–300 °C adjacent to the focal point location, enabling the cooker to cater frying and grilling requirements unlike box-cookers adequate only for boiling-type cooking requirements.

Primary paraboloid reflector coupled with secondary reflector PCM solar cooker: Since the positioning of heavy cooking cum storage vessel over the paraboloid reflector poses considerable challenge with respect to the solar tracking requirement, arrangement of a double reflector-based design (Fig. 5) is proposed to circumvent this challenge Veremachi et al. (2016). The key feature of this design is the positioning of a secondary reflector close to the focal point of the primary reflector. The primary reflector is a paraboloid reflector which reflects solar radiation onto the secondary reflector. The secondary reflector concentrates the radiation on the storage container during the charging process. A hole at the center of the primary reflector allows the radiation from the secondary reflector to reach the storage container kept beneath the primary paraboloid reflector. This setup is ergonomically more viable for solar tracking operation as the heavy storage container sits at bottom most location. Another advantage of this mechanism is obtaining a fixed hotspot location on the storage container during charging process which is otherwise very difficult to obtain with single reflector design. However, for this design, simultaneous cooking and charging operation is limited to boiling type of cooking only. Cooking requirements

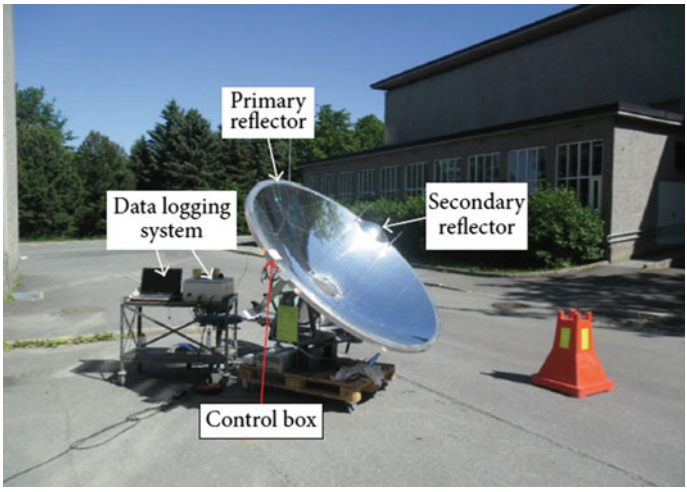

Fig. 5 Primary and secondary reflector solar cooker Veremachi et al. (2016)

like frying or grilling can only be addressed once the charging process of the storage unit is over.

Next, we briefly discuss some of the existing designs of indirect solar cookers. Unlike direct solar cookers solar irradiation is not directly used for cooking or energy storage, rather a heat transfer fluid (HTF) is used as the thermal transport medium to transfer heat from the receiver to the cooking cum storage unit. The thermic fluid is continuously circulated between the receiver and storage cum cooking unit during the cooking and storage operation. Three types of receivers are particularly of interest, namely evacuated tube, parabolic trough, and flat plate collector.

Evacuated tube solar cooker: Fig. 6 depicts the key components of solar cooker with an evacuated tube receiver (Sharma et al. 2005). The evacuated tube consists of an inner metallic pipe encased within a transparent glass tube. The exterior surface of the inner metallic tube is coated with a solar selective coating having high absorptivity and low emissivity. Vacuum is maintained within the gap between the inner metallic tube and an outer glass tube to protect the solar selective coating from degradation due to contact with air. The arrangement also ensures minimum heat loss through convection and radiation mechanism. During on-sun hours, solar radiation is absorbed by the evacuated tube solar collector, and heat is transferred to the HTF circulating through the heated tube. The HTF circulation is achieved using a closed-loop pumping setup. The pump drives the HTF in a close loop through a steel tubing arrangement wrapping around the storage cum cooking container and the evacuated tube receiver. Once again the storage cum cooking container is a double-walled vessel with the gap between the two walls filled with PCM. The HTF circulation system passes through this PCM-filled domain. The HTF circulation loop transports heat from the evacuated receivers to the storage cum cooking container. The flow of hot HTF through the PCM causes the melting of PCM and stores heat in PCM in the

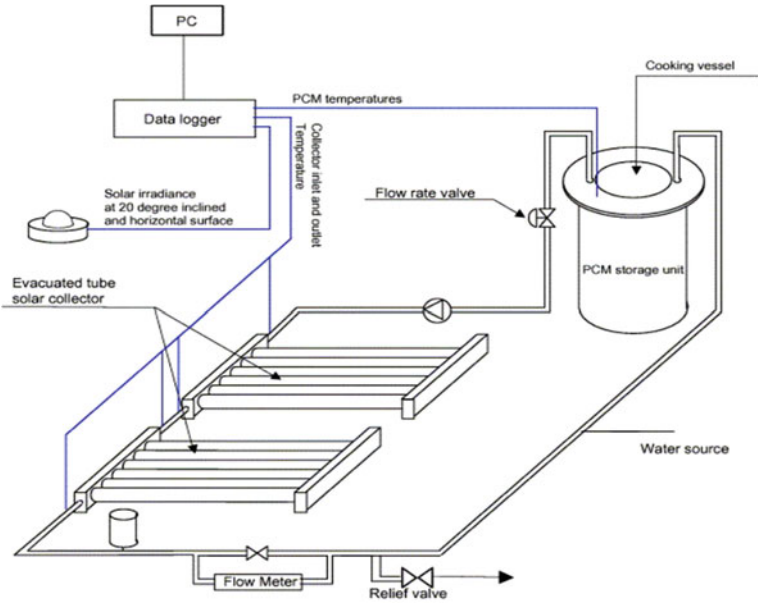

Fig. 6 Schematic diagram of evacuated tube solar cooker with LHTES (Sharma et al. 2005)

form of latent heat, which can be used for cooking at later duration. The absence of solar irradiation concentrator restricts this system to attain high temperature and confines the temperature below 100 °C. Additional pump setup, flow meter, relief valves, and electrical power are required for this closed-loop setup.

Parabolic trough solar cooker: The functionalities of a solar cooker with parabolic trough as the receiver is quite similar to the evacuated tube solar cooker. The only difference between the two being receiver type. However, owing to the usage of a parabolic concentrator, the very high HTF temperature can be achieved by using multiple parabolic concentrators. The performance of this solar cooker can be further improved by using a combination of evacuated tube and parabolic reflector. The schematic of such an arrangement is shown in Fig. 7 (Kumaresan et al. 2015, 2016).

Flat plate collector PCM solar cooker: This setup consists of a flat plate solar collector through which the HTF is circulated (Fig. 8) before delivering the heat to the cooking cum storage container containing PCM as storage material similar to the evacuated tube and parabolic trough solar cooker systems. Once again the absence of concentrator limits the obtainable temperature below 100 °C.

Classification of PCMs used for solar cookers

Several types of PCM have been explored by research groups across the globe as latent heat thermal energy storage medium for solar cooking applications. A consolidated list of PCMs used as thermal energy storage medium for cooking application is shown

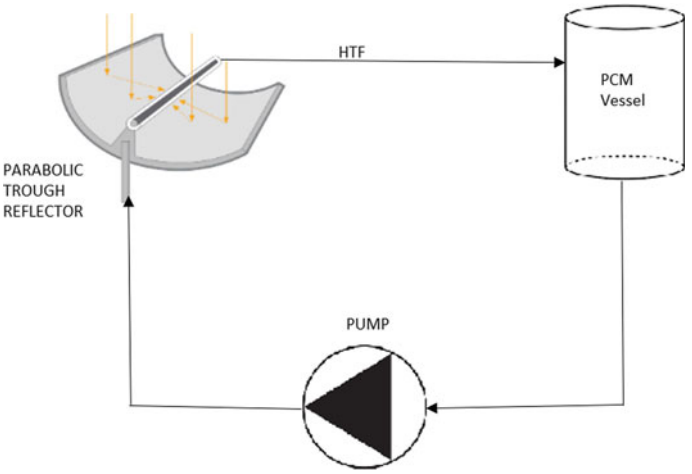

Fig. 7 Schematic diagram of parabolic trough solar cooker with heat transfer fluid

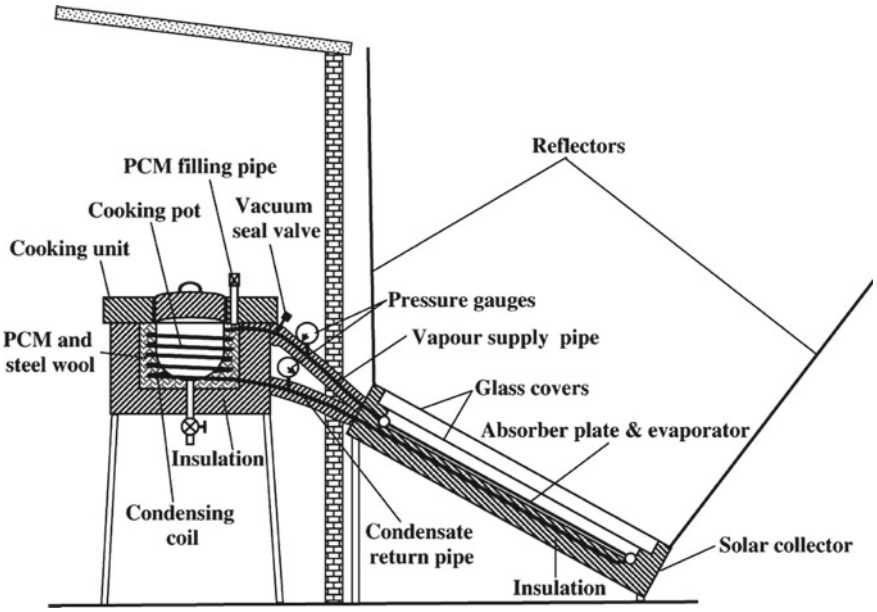

Fig. 8 Schematic diagram of flat plate collector PCM solar cooker (Hussein et al. 2008)

in the chart presented by Figs. 9 and 10. The pros and cons of organic, inorganic, and eutectic PCMs are listed in Table 1.

Selection standards for PCM used in the PCM solar cooking device: There are specific features to be addressed while choosing PCM as thermal storage medium

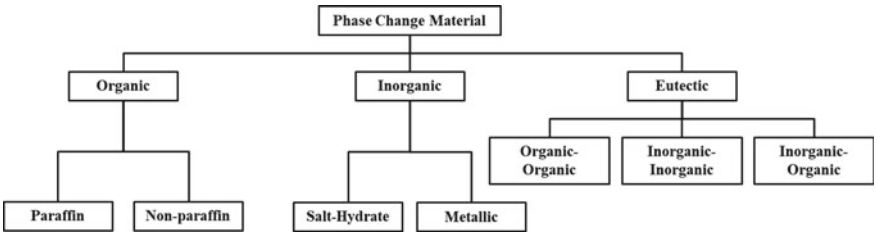

Fig. 9 Classification of PCM (Memon 2014)

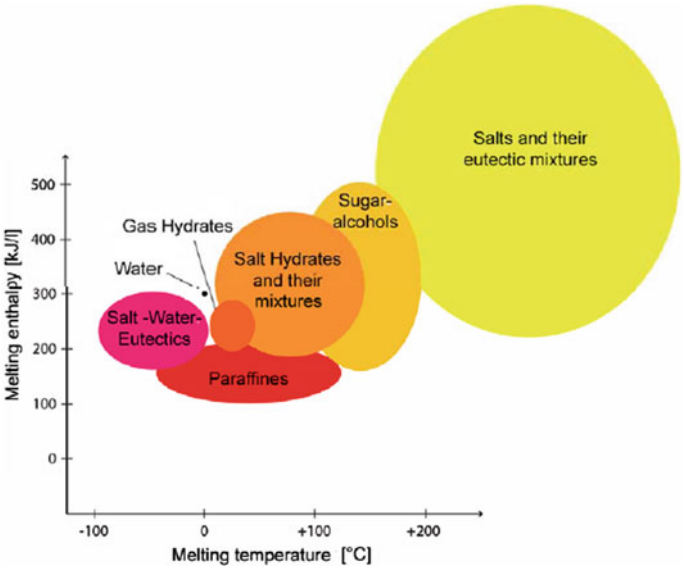

Fig. 10 Fusion enthalpy (kJ/l) versus melting temperature (°C) of various types of PCMs (Kalnæs and Jelle 2015)

for solar cooking application. The preferable features can be summarized as follows (Memon 2014):

A. **Thermophysical features**

1. Large energy storage density to ensure a compact storage unit
2. Reasonably high thermal conductivity to achieve rapid charging process and maintain thermal uniformity and rapid heat flow during cooking or discharging process
3. Large specific heats for solid and liquid phase also ensure higher storage density
4. Small volumetric changes during phase transitions allow simple design requirement for storage container

Table 1 Merits and demerits of organic, inorganic, and eutectic PCMs

PCM type	Merits	Demerits
Organic	• Significant deviation (from 20 to 70 °C) in phase change temperature • Chemically dormant • Better thermal steadiness in a long run melt cycle • Intermediate latent heat of fusion (120–210 J/g) • Superior thermal specific heat in comparison to inorganic PCM • Usually non-corrosive • Economically viable • Compatibility with commonly available container materials excluding plastics • Variation in volume at the time of phase change process is minimal • Minor supercooling during solidification • Usually safe environmentally • Mostly stable at temperatures under 500 °C • Replenishable	• Low melting point • Reasonably small thermal conductivity (about 0.21 W/mK) • Moderately flammable
Inorganic	• Latent heat storage capacity is twice in comparison to organic PCMs • High latent heat of fusion • Thermal conductivity is generally much higher than organic PCM (about 0.5 W/mK) • Economical and readily accessible • Fire resistant • Affinity for plastic container • Small changes in volume on melting • Potentially recyclable • Insignificant solubility in water	• Prone to endure supercooling during freezing • High probability of phase segregation during freezing • Corrosive nature to most metals
Eutectic	• Transformation of phase is at a constant temperature • Energy stored per unit volume is marginally higher than the organic PCM	• Data on the thermophysical properties are not broadly available

5. Thermal stability of PCM and low degradation rate allow a large number of thermal cycles and infrequent replacement requirement for thermal storage material.

B. **Chemical features**

1. The chemical composition must remain stable and uniform over a large number of thermal cycles involving phase change process

2. PCM must be non-toxic, non-corrosive, and non-explosive.

C. **Economic features**

1. The material used for the storage medium must be inexpensive
2. Readily accessible.

D. **Environmental features**

1. The PCM must be non-contaminating
2. The PCM must be easily replenishable.

Thermophysical properties of some commonly used and potential PCMs for solar cooking applications are enlisted in Table 2.

Although discussions regarding design aspects of box-type solar cookers with latent heat storage are frequently encountered (Domanski et al. 1995; Buddhi and Sahoo 1997; Buddhi et al. 2003; Vigneswaran et al. 2017; Coccia et al. 2018), and reports on dish concentrator-based solar cookers with latent heat storage are rarely available (Bhave and Thakare 2018; Foong et al. 2010). In the subsequent section, we provide a detailed modeling description of double reflector-based parabolic dish solar cookers integrated with latent heat storage unit.

2 Design Details of Double Reflector-Based Parabolic Solar Cooker Integrated with Latent Heat Storage Unit

In order to store sufficient thermal energy to cook meal for a family, the total weight requirement of the thermal storage medium is quite high (~10 kg). The weights of the container and insulation material are added over it. Placing this heavy storage unit above the parabolic dish concentrator poses serious structural constraint. For any practical purpose, such top heavy arrangement is not desirable. Continuous solar tracking requirement for the parabolic dish concentrator complicates the matter farther. Locating the bulky storage structure above, the concentrator also restricts a significant amount of sunlight to reach the parabolic dish reflector due to the shadow effect. All these structural and optical challenges can be comprehensively addressed by an alternative design approach of locating the storage unit below the parabolic dish concentrator with double reflector arrangement. Figure 11 shows such an arrangement. The solar irradiation captured by the primary reflector is first focussed on a much smaller secondary reflector (Fig. 11), which directs the focussed solar rays on the storage container located below the primary reflector. A small hole at the center of the primary reflector allows the rays from the secondary reflector to pass through and incident on the latent heat storage container. The large primary reflector is a parabolic dish and the secondary smaller reflector is a hyperbolic dish. The design constraints of these two reflectors are briefed in the subsequent discussions.

Primary and secondary reflector design: Solar energy received from the solar irradiation needs to be concentrated to receive high heat flux at high temperature in

Table 2 Property table for potential PCMs for solar cooking application

PCM	H (kJ/kg)	T_m (°C)	ρ (kg/m^3)		c_p (kJ/kg K)		k (W/mK)		μ (Ns/m^2)	References
			S	L	S	L	S	L		
Paraffin	140	100	880	770	1.8	2.4	0.21	0.2	0.049	Bhave and Thakare (2018)
Erythritol	340	118	1480	1300	1.38	2.76	0.733	0.326	0.01	Bhave and Thakare (2018)
Stearic acid	157	54	940	–	1.76	2.27	0.29	0.17	–	Sarbu and Dorca (2019)
Manganese nitrate hexahydrate	280	89	1640	–	2.5	3.1	0.65	0.5	–	Sarbu and Dorca (2019)
Commercial-grade acetanilide	118.9	222	1318	–	2.00	–	–	–	–	Buddhi et al. (2003)
53 wt% KNO_3,40 wt%$NaNO_2$, 7wt% $NaNO_3$	145.14	101.50	–	–	1.441	1.462	–	–	–	Coccia et al. (2018)
D-mannitol	300	165	1490	–	1.31	2.36	0.19	0.11	–	Sarbu and Dorca (2019)
Oxalic acid	356	105	1900		1.62	2.73	–	–	–	Mukherjee (2018)
Magnesium chloride hexahydrate	117	167	1450	1570	2.61	2.25	0.570	0.704	–	Sarbu and Dorca (2019)
Acetamide	260	82	1160	–	2.00	3.00	0.4	0.25	–	Mukherjee (2018)

H = latent heat of fusion, T_m = melting point temperature, ρ = density, c_p = specific heat capacity, k = thermal conductivity, μ = dynamic viscosity

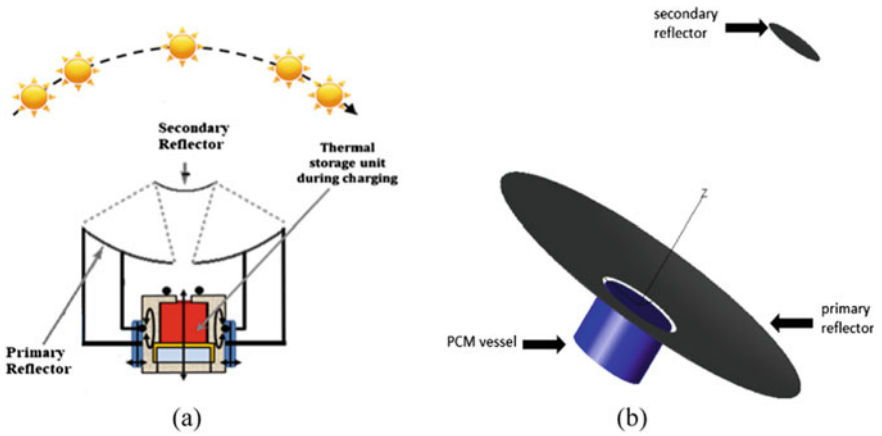

Fig. 11 Schematic diagram of double reflector-based high temperature thermal storage arrangement, **a** 2-D view, **b** 3-D view

the designated receive location of the storage container. The primary and secondary reflector arrangement ensures the concentration of high heat flux at a reasonably high temperature ($\sim$ 350 °C) to be incident on the receiver location of the storage container. To design the reflectors, we require the knowledge of total thermal energy for cooking (E_c) the target meal proportion, target charging duration (Δt_{ch}) of the thermal storage unit, average local DNI (I), and the maximum temperature ($T_{\max} > T_m$) attainable by the PCM without degrading. Once the total requirement of energy for cooking and charging duration is identified, the incident area (A) of the primary reflector can be estimated from the following relation.

$$E_c = I \cdot A \cdot \Delta t_{\text{ch}} \cdot \alpha \tag{1}$$

where α represents the absorptivity of the vessel surface.

Average cooking energy (E_c) requirement above 100 °C for a six-member family is typically 1.2–1.5 kWh (Buddhi et al. 2003). The average DNI observed at Jodhpur is approximately 600 W/m^2. However, to be on the safer side, an average DNI of 450 W/m^2 is considered. Typically, the aperture diameter of the parabolic dish reflector varies within the range of 1.2–2 m. On the other hand, the target charging time should ideally be less than 5 h. A safe value of absorptivity (α) can be assumed to be 85%. Considering all these facts, and taking into account of central hole and shadow effect of the structural frame to support the secondary reflector, Eq. 1 can provide an accurate diameter requirement of the primary reflector. TracePro ray tracing software is used for designing the primary (paraboloid) and secondary (hyperboloid) reflectors (Fig. 12) along with the incident heat flux distribution on the receiver area of the thermal storage container.

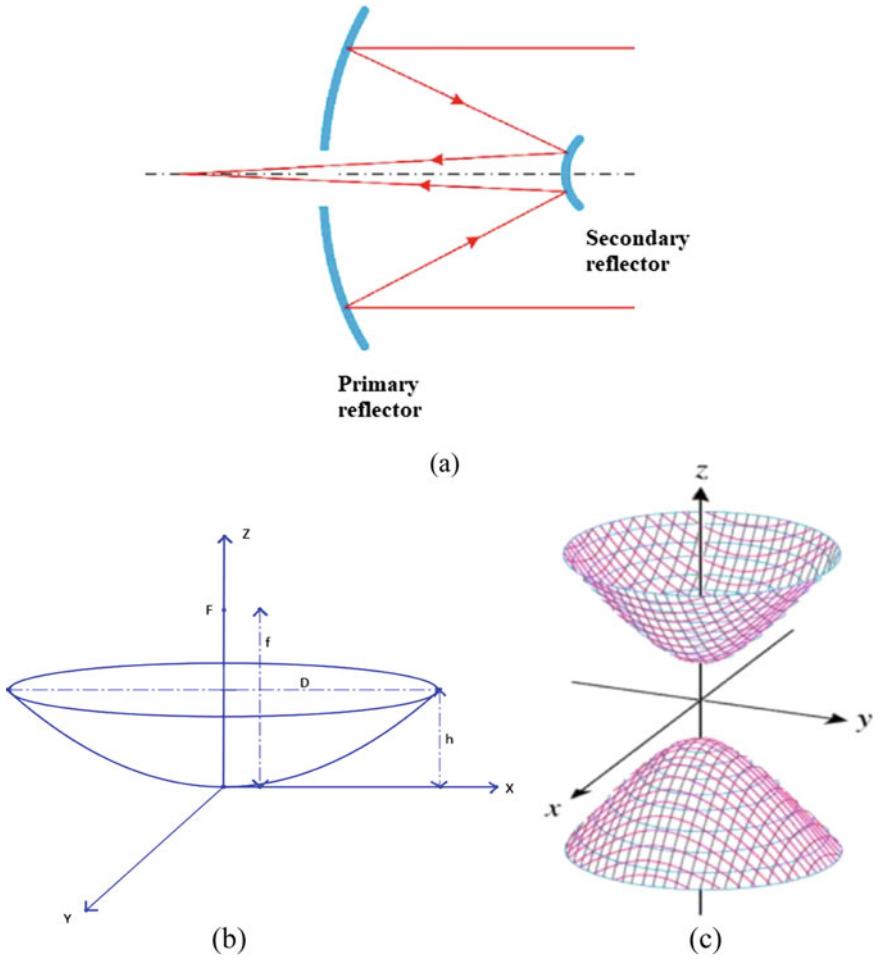

Fig. 12 **a** Light path of Cassegrain model; graphical definition of the **b** paraboloid, **c** hyperboloid reflectors

The 'classic' Cassegrain reflector model is considered for concentrating solar energy (Fig. 12a). A hole is made in the center of the paraboloid reflector to allow the rays to pass through to the receiver location of the thermal storage container. The hyperboloid is kept above the primary reflector and aligned along the same vertical axis of the paraboloid. The sun rays are reflected from the primary paraboloid reflector to the secondary hyperboloid reflector, which in turn concentrates solar radiation upon the cooking vessel. The paraboloid reflector reflects all incoming light rays parallel to its axis of symmetry toward a single point, the focus. The converging light rays reflected by the parabolic concentrator toward its focus are intercepted by a secondary hyperboloid reflector. The hyperboloid reflector surface having two

foci reflects all light rays directed toward one of its two foci in the direction of its other focal point (Fig. 12a). The folded optical path in this manner results in a very compact system; hence, hyperboloid geometry is considered for the secondary reflector (Horne 2012). The light rays reflected from the hyperboloid need not be parallel. This novel design helps in decreasing the shadow effect since the aperture of the hyperboloid is considerably smaller than the radial span of the storage container. This bottom heavy arrangement also facilitates structural stability and ergonomics of the storage cum cooking container.

Recalling the basic features of paraboloid geometry, the curved surface formed by rotation of a parabola about its axis is called a paraboloid of revolution. The mathematical equation for the paraboloid (Fig. 12b) in Cartesian coordinate system with the z-axis as the axis of the paraboloid is as follows.

$$x^2 + y^2 = 4fz \tag{2}$$

where the distance f is the focal length.

In cylindrical coordinates, the equation becomes:

$$z = \frac{r^2}{4f} \tag{3}$$

The aperture area of the paraboloid is given by:

$$A_p = \frac{\pi D^2}{4} \tag{4}$$

where D is the aperture diameter.

In terms of aperture diameter and focal length, the height of the dish h is:

$$h = \frac{D^2}{16f} \tag{5}$$

The surface area of the paraboloid is given by:

$$A_s = \frac{8\pi f^2}{3}\left\{\left[\left(\frac{D}{4f}\right)^2 + 1\right]^{3/2} - 1\right\} \tag{6}$$

Concentration ratio is defined as the ratio of aperture area of the concentrator to the focal area of the receiver.

$$\mathrm{CR} = \frac{A_p}{A_r} \tag{7}$$

where A_p denotes the aperture area of the concentrator and A_r denotes the focal area on the receiver surface.

Collector Efficiency
The solar energy collection efficiency η_{col} of thermal collectors is defined as the ratio of the rate of useful thermal energy leaving the collector, to the useable solar irradiance falling on the aperture area. Simply stated, collector efficiency is

$$\eta_{\text{col}} = \frac{Q_{\text{useful}}}{A.I}$$

Optical Efficiency of Collector
Optical efficiency is formulated as

$$\eta_{\text{opt}} = \tau \cdot \alpha$$

where τ is the transmittance of reflector glass and α is the absorptivity of receiver surface.

Recalling the hyperboloid geometry the equation representing a hyperboloid in Cartesian coordinate system is given by:

$$\frac{x^2}{a^2} + \frac{y^2}{b^2} - \frac{z^2}{c^2} = -1 \tag{8}$$

The intercepts of the hyperboloid with z-axis is given by (0, 0, $\pm c$). There are no intersections with the x, y-axes.

Design of thermal storage container: Dimensions of the storage container are obtained on the basis of the required cooking energy to be stored above 300 °C. We chose the total cooking energy requirement to be 1.5 kWh which is sufficient to cook a sumptuous Indian style meal for a six-member family (Buddhi et al. 2003). A cylindrical steel vessel of wall thickness 3 mm is considered. A ceramic coating of 2 mm thicknesses on the inner surface of the steel container is also considered. Ceramic coating is considered to prevent the corrosive effect of molten PCM at elevated temperatures on the steel container (Moreno et al. 2014). However, steels with anticorrosive properties are available, and thermal storage container made with such corrosion resistant steel may not require this protective ceramic layer.

Two different designs for thermal storage container are considered for the present study (Fig. 13). The first design (Fig. 13a) consists of a cylindrical steel vessel without fin arrangement, while the second design (Fig. 13b) involves a cylindrical steel vessel with circumferentially distributed copper fins. For the finned design of thermal storage vessel, the central copper rod is of diameter 10 mm, and each of the radially extended copper plates from the central rod has a thickness of 2 mm.

Selection of PCM material: In the present study, $NaNO_3$-CEG (sodium nitrate-compressed expanded graphite) composite is used as latent heat storage medium

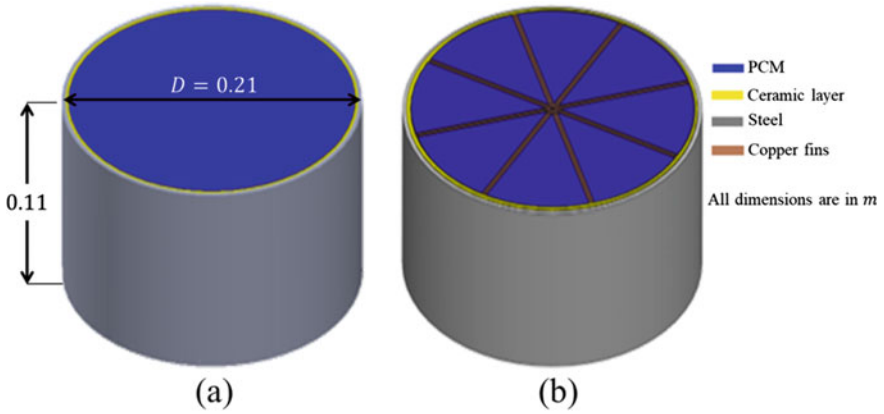

Fig. 13 Schematic diagram of storage container, **a** without fin, **b** with circumferentially distributed fins

with a melting temperature of 308 °C. The major drawback of pure $NaNO_3$ is that its low thermal conductivity (0.5 W/mK) causing accumulation of heat near the receiver area of the storage container. If pure $NaNO_3$ is used as the latent heat storage medium, the low thermal conductivity causes a large temperature gradient within the storage medium with a local hotspot near the receiver region. Very high temperature (∼400 °C) at the hotspot may lead to decomposition of nitrate to nitrite and degrade the thermal properties of $NaNO_3$. Therefore, enhancement of thermal conductivity is of absolute necessity for such high-temperature application. The thermal conductivity of $NaNO_3$ is enhanced by incorporating 10% graphite by volume in the form of compressed expanded graphite (CEG). $NaNO_3$-CEG composite consists of a highly porous CEG matrix impregnated with $NaNO_3$. The thermal conductivity of $NaNO_3$-CEG is higher by two orders of magnitude as compared to pure $NaNO_3$ (Kenisarin 2010). Incorporating graphite in PCM results in anisotropic thermal conductivity in the PCM domain. An interesting aspect of PCM-CEG composite is that natural convection does not play a dominant part in the heat transfer and is dominated by heat diffusion only (Py et al. 2001). The small pore size of CEG matrix allows the composite to be analyzed as a homogeneous material. The thermophysical properties have been estimated using volume averaging approach. Homogeneous distribution assumption of very small pore size allowed us to consider this volume averaged estimation of thermal conductivity approach with reasonable accuracy (Mallow et al. 2016). The major limitation of this approach is negating the existence of thermal non-equilibrium between the graphite and PCM due to large difference in thermal conductivities of these two materials. Inclusion of thermal non-equilibrium effect between the graphite and PCM in the numerical model is beyond the scope of the present work and needs to be explored farther providing a future scope for the present study. Based on the volume calculation of the storage container, the total weight of $NaNO_3$ content is approximately 7 kg, which is capable of storing approximately 1.2

Table 3 Thermophysical properties of container material, PCM (Venkateshwar et al. 2017), and CEG (Bodzenta et al. 2011)

Material	c_p(kJ/kg K)	k(W/mK)	$\rho\left(\text{kg/m}^3\right)$	T_m(°C)	h_{sl}(kj/kg)
PCM	1.820	0.5	2260	308	172
CEG	1.820	11 (axial) 42.3 (radial)	2250	–	–
SS	0.502	16.27	8030	1577	–
Copper	0.381	387.6	8978	1085	–

kWh energy above 100 °C. Thermophysical properties of container material, PCM (Venkateshwar et al. 2017), and CEG (Bodzenta et al. 2011) are provided in Table 3.

3 Numerical Modeling

In this section, we present the numerical model to capture storage dynamics during the charging cycle. The first step in this endeavor is to evaluate incident flux distribution on the receiver region of the thermal storage container. Once this incident flux profile is obtained, it is used as the boundary condition to solve the energy conservation equation in the storage domain.

Incident flux profile: The incident heat flux profile is obtained by using ray tracing TracePro software (Figs. 14 and 15). Average DNI data measured at IIT Jodhpur is used as the input to the software for attaining irradiation flux profile on the receiver surface. The flux profile obtained follows Gaussian distribution.

The incident flux profile $q(r)$ on the PCM vessel is formulated as

$$q(r) = A_1 e^{\left(\frac{r-b_1}{c_1}\right)^2} + A_2 e^{\left(\frac{r-b_2}{c_2}\right)^2} + A_3 e^{\left(\frac{r-b_3}{c_3}\right)^2} + A_4 e^{\left(\frac{r-b_4}{c_4}\right)^2} \tag{9}$$

where $A_1, A_2, A_3, A_4, b_1, b_2, b_3, b_4, c_1, c_2, c_3, c_4$ are discrete functions of time which remain constant for each time intervals of 20 min. MATLAB has been used to obtain the approximate Gaussian distribution (Eq. 9) from the solar irradiance data with uncertainty of less than 5%.

Numerical modeling: The governing energy balance equation for the PCM-CEG domain is derived on the basis of volume averaging formulations proposed by Brent et al. (1988), Bennon and Incropera (1987), and Shrivastava and Chakraborty (2019). Since the PCM is trapped within the porous matrix of CEG in the composite, convection within PCM melt is neglected and the energy balance equation is diffusion dominated. In deriving the energy balance equation, the difference between specific heat capacities of solid and liquid phases of PCM is considered (Shrivastava and

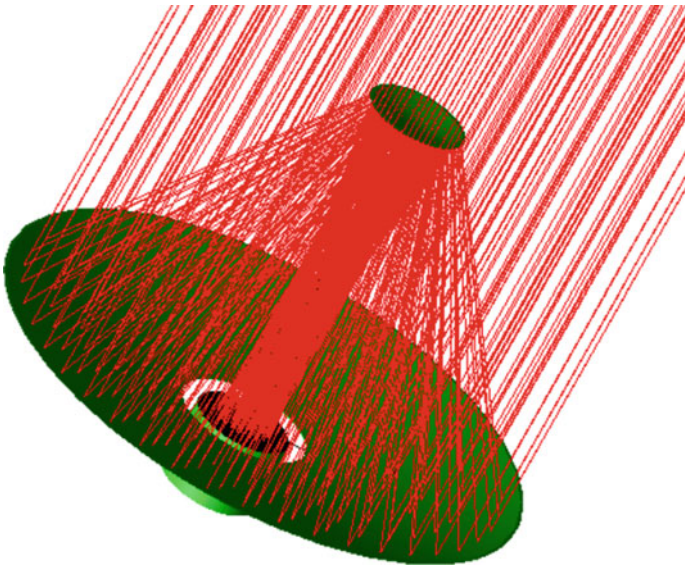

Fig. 14 Ray tracing diagram of the double reflector system

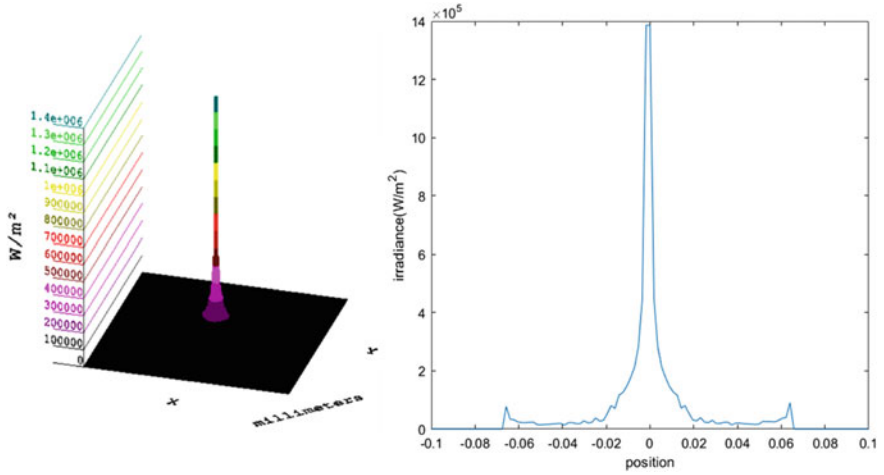

Fig. 15 Flux profile obtained in Ray Tracepro software

Chakraborty 2019). The sensible heating of graphite matrix is also considered (Shrivastava and Chakraborty 2019). The energy conservation equation in the PCM-CEG composite domain using temperature as the primary dependent variable can be formulated as follows (Shrivastava and Chakraborty 2019):

$$\frac{\partial(T)}{\partial t} = \nabla.\left(\frac{k}{\rho c_{ps}}\nabla T\right) - \frac{\partial}{\partial t}\left(\frac{g_l h_{sl}}{c_{ps}}\right) - \frac{\partial}{\partial t}\left[g_l\left(\frac{c_{pl}}{c_{ps}} - 1\right)(T - T_m)\right] - \frac{\partial}{\partial t}\left[g_g\left(\frac{c_{pg}}{c_{ps}} - 1\right)T\right] \tag{10}$$

The second, third, and fourth source terms appearing on the right-hand side of Eq. 10 represent contributions due to phase change, difference between liquid and solid phase specific heats of PCM and difference between graphite and solid phase PCM specific heat, respectively. Since the graphite matrix has anisotropic thermal conductivity, the effective thermal conductivity (k) is defined in the following manner (Shrivastava and Chakraborty 2019).

$$k_i = g_l k_l + g_s k_s + g_{g,i} k_{g,i} \tag{11}$$

where subscript i represents (r, x) direction in cylindrical coordinate system, subscripts l, s represents liquid and solid phases of PCM, and subscript g represents graphite.

The energy equation for ceramic, steel, and copper fin regions is formulated as follows.

$$\frac{\partial}{\partial t}(T) = \nabla.\left(\frac{k}{\rho c_p}\nabla T\right) \tag{12}$$

Heat loss from the circumferential surface and bottom surface is assumed to be zero, i.e., these surfaces are considered to be perfectly insulated. The surface area of the storage container pertaining to the receiver location is provided with the heat flux boundary condition given by Eq. 9.

Volume fraction updating scheme is implemented to estimate the liquid volume fraction using the following updating scheme (Shrivastava and Chakraborty 2019)

$$g_{lp}^{n+1} = g_{lp}^{n} + \lambda\left[\left\{\frac{A_p + D_p + C_p g_{lp}^{n}}{B_p}\right\}(T - T_m)\right] \tag{13}$$

where subscript p represents the nodal point where volume fraction g_l is being updated. A_p represents coefficient of T_p obtained by finite volume discretization of Eq. 10 (Patankar 2018) when contribution of only left-hand side and first term (diffusion term) of the right-hand side of Eq. 10 is considered (Chakraborty 2017). λ is an under-relaxation factor. Superscripts 'n' and '$n + 1$' denote iteration steps during implicit calculation of T and g_l field at a given time step. B_p, C_p and D_p are given as follows:

$$B_p = \frac{h_{sl}}{c_{ps}}; \quad C_p = \frac{c_{pl}}{c_{ps}} - 1; \quad D_p = g_g\left(\frac{c_{pl}}{c_{ps}} - 1\right) \tag{14}$$

The liquid volume fraction g_l ranges within the limit: $0 \leq g_l \leq 1 - g_g$, where g_g represents volume fraction of graphite at an elementary control volume. If the numerical value of g_{lp}^{n+1} from Eq. 13 comes outside the range $0 \leq g_l \leq 1 - g_g$, it is updated as the nearest limit such that:

$$\begin{aligned} g_{lp}^{n+1} &= 0 \qquad \text{for } g_{lp}^{n+1} < 0 \\ g_{lp}^{n+1} &= 1 - g_g \text{ for } g_{lp}^{n+1} > 1 - g_g \end{aligned} \tag{15}$$

Since the energy equation solved by ANSYS-FLUENT solve (Fluent ANSYS 2015) either enthalpy or total energy as primary variable, Eq. 1 could only be solved by treating temperature T as the user-defined scalar (UDS). The enthalpy updating scheme is applied through user-defined function. The anisotropic thermal conductivity (Eq. 11) and the heat flux boundary condition (Eq. 9) are also implemented through UDFs. A grid size of 1 mm has been used for numerical simulations followed by 0.5 s time step.

4 Results and Discussions

The thermal storage dynamics during the charging process is studied for two different sets of storage configurations. The first configuration consists of thermal storage container without any fin arrangement inside the PCM-CEG domain (Fig. 13a). The second configuration contains circumferentially distributed copper fins within the storage medium (Fig. 13b).

Case study 1 (Thermal storage container without fin): This study could have been performed for 2-D axisymmetric geometry. However, the other case study involving circumferentially oriented fin cannot be resolved with 2-D axisymmetric simplification, and a 3-D approach is a must. The 3-D domain can however be reduced conveniently because the fins are oriented with regular angular intervals. In order to have a better comparison with the finned configuration, the case study involving unfinned thermal storage container is carried out in 3-D domain. One-eighth symmetry with an angular span of 45° (Fig. 16) is chosen as the reduced domain for case study 1 in order to reduce total computation time.

The initial temperature of the complete system is assumed to be at ambient temperature 27 °C. The charging process of the PCM is carried out between 10 am to 1:20 pm, i.e., for 3 h and 20 min since the average DNI in this period is maximum. The maximum temperature attained in the system during charging after 12,000 s is 374 °C (647 K) which is tantalizingly close to the temperature 380 °C at which decomposition of $NaNO_3$ in $NaNO_2$ starts. The minimum temperature of the storage medium is found to be 303 °C (5 °C below the melting point temperature $T_m = 308$ °C of $NaNO_3$) indicating incomplete melting of the storage medium.

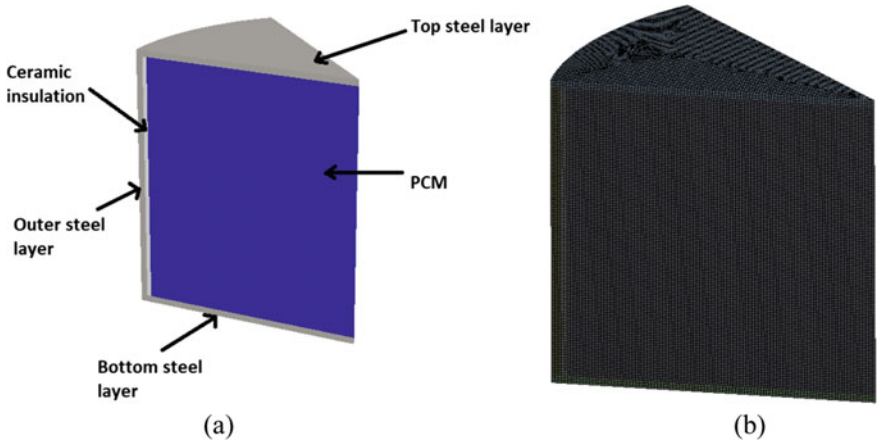

Fig. 16 Computational domain for no-fin storage container configuration, **a** schematic diagram, **b** hex mesh generated in ANSYS

The temperature profile evolution in time for the PCM-CEG domain within the storage unit is presented in Fig. 17 at various time intervals. The solar irradiation flux profile at the receiver region of the CEG-PCM thermal storage container is such that it creates a hotspot at the center of the vessel top surface. The non-uniform temperature distribution (Ranging over a temperature difference of ~30 to 70 °C at different time instants) within the PCM may be attributed to the low thermal conductivity of the PCM. The melting fraction evolution is shown in Fig. 18 at the same time intervals 9000, 10,000, 11,000, and 12,000 s. It is to be noted from Fig. 18, that melting of the PCM starts at around 10,000 s. The complete melting is achieved at 12,100 s, and the time required for complete melting is around 2100 s. One of the interesting non-intuitive features of the melting dynamics is found to be the location where melting process occurs at the end. We found that the location where the melting process defers till the end is adjacent to the central region of the storage container (Fig. 18d) and not the farthest region from the hotspot or receiver area. The reason for this non-intuitive melting feature is attributed to the fact that steel having reasonably larger thermal conductivity (~16 W/mK) carries the heat from the hotspot along the container wall, promoting faster meltdown of the PCM adjacent to the wall. On the other hand, comparatively low thermal conductivity of CEG in the axial direction due to anisotropy causes slower heat transfer from the hotspot in the axial region, rendering the central region of the storage container not to reach melting temperature till the very end.

Case study 2 (Thermal storage container with fin arrangement): Case study with fin arrangement consists of three subsystem studies with three different fin orientations in the circumferential direction. These three different fin configurations consists of radially extended copper plane plate fins attached to a central copper rod with an angular pitch of 30°, 45°, and 60°. The schematic of 45° fin orientation

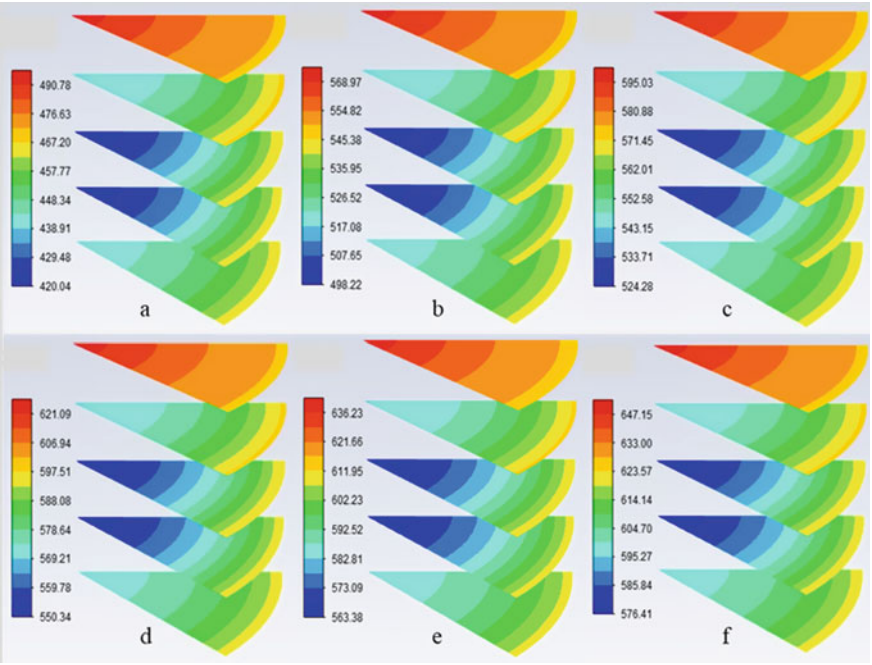

Fig. 17 Temperature (Kelvin) profile of PCM-CEG domain without fin at: **a** 6000 s, **b** 9000 s, **c** 10,000 s, **d** 11,000 s, **e** 11,500 s, and **f** 12,000 s

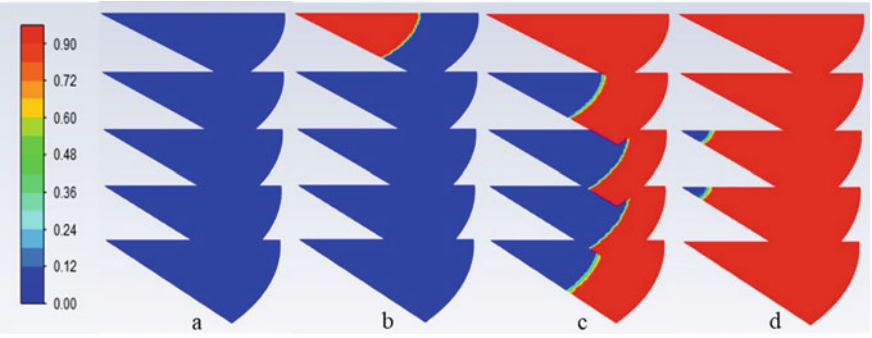

Fig. 18 Melting fraction profile of PCM-CEG domain without fin at: **a** 9000 s, **b** 10,000 s, **c** 11,000 s, **d** 12,000 s

is presented in Fig. 19a. Since the fins are located at regular angular intervals, the computation domain can be reduced comprehensively by considering the volume enclosed by two consecutive fins. Figure 19b shows the computation domain for 45° fin orientation. Figure 20 shows the mesh generated in ANSYS for three different

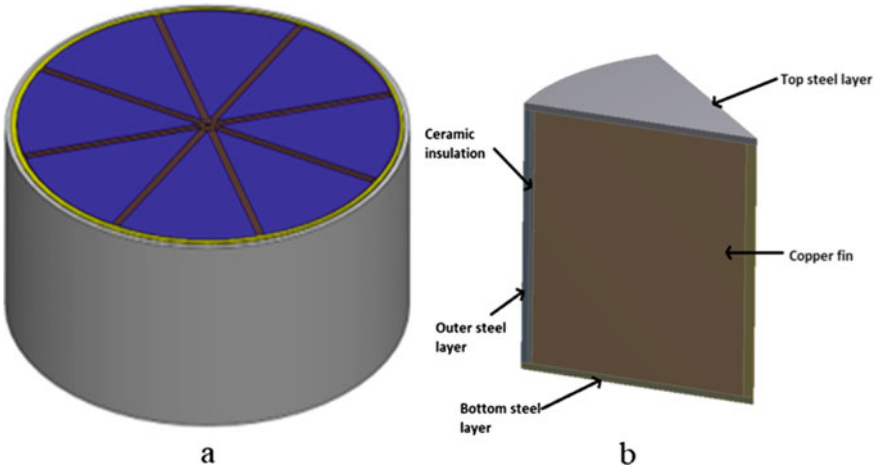

Fig. 19 **a** Schematic diagram of thermal storage container with 45° fin orientation, **b** reduced computational domain for 45° fin orientation

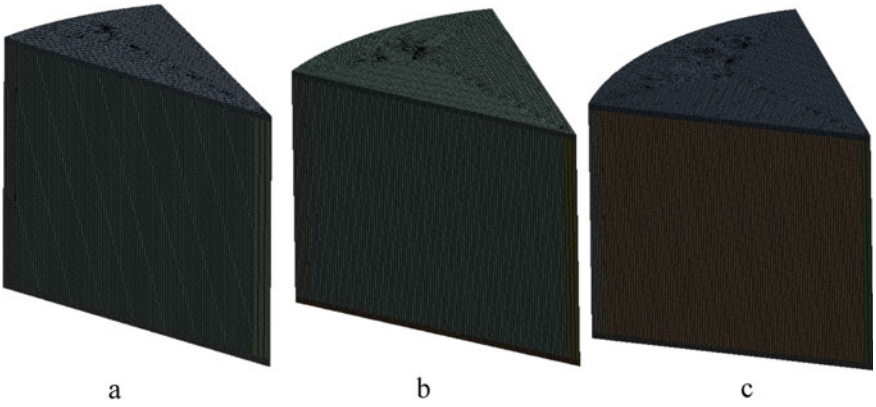

Fig. 20 Hex mesh generated in ANSYS for: **a** 30°, **b** 45°, and **c** 60° fin orientations

fin arrangements. The charging process starts at 10 am and is carried out for 3 h and 20 min from the start time.

Once again, the initial temperature of the complete system for all the cases is assumed to be at ambient temperature 27 °C Figs. 21, 22, 23, 24 and 25 represents temperature profile and melt fraction evolution in time for the PCM-CEG domain within the storage unit for fin orientation of 30°, 45°, and 60°, respectively. When the temperature profiles of finned containers (Figs. 21, 23 and 25) are compared with that of non-finned case study, we find that the difference between the highest and lowest temperature within the PCM-CEG domain is much smaller (∼10 °C for 30°, ∼13 °C for 45°, and ∼16 °C for 60° fin orientations, respectively) indicating much better

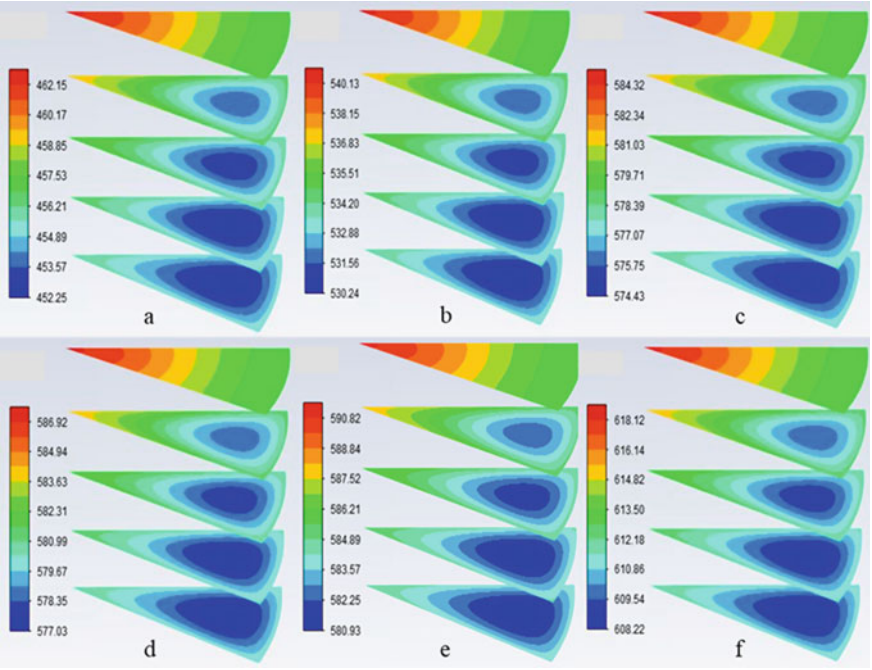

Fig. 21 Temperature (Kelvin) profile of PCM-CEG domain for 30° fin orientation at: **a** 6000 s, **b** 9000 s, **c** 10,700 s, **d** 10,800 s, **e** 10,950 s, and **f** 12,000 s

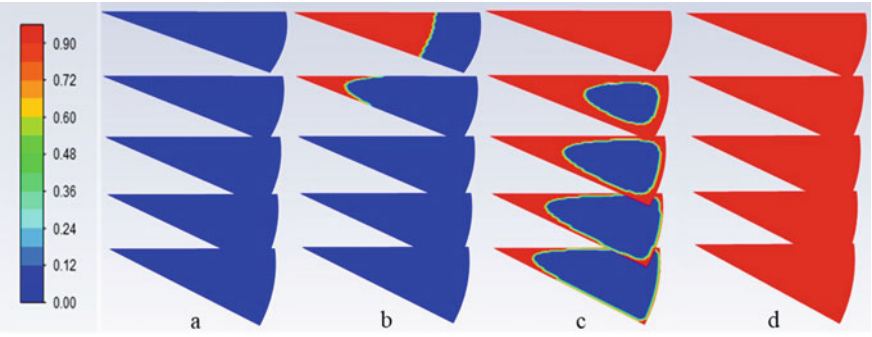

Fig. 22 Melting fraction profile in PCM-CEG domain for 30° fin orientation at: **a** 9000 s, **b** 10,700 s, **c** 10,800 s, and **d** 10,950 s

uniformity of temperature within the storage medium. The temperature maximums at 12,000 s are also found to be significantly lower (345, 339 and 335 °C for 30°, 45°, and 60° fin orientations, respectively) than the decomposition temperature (380 °C) of $NaNO_3$.

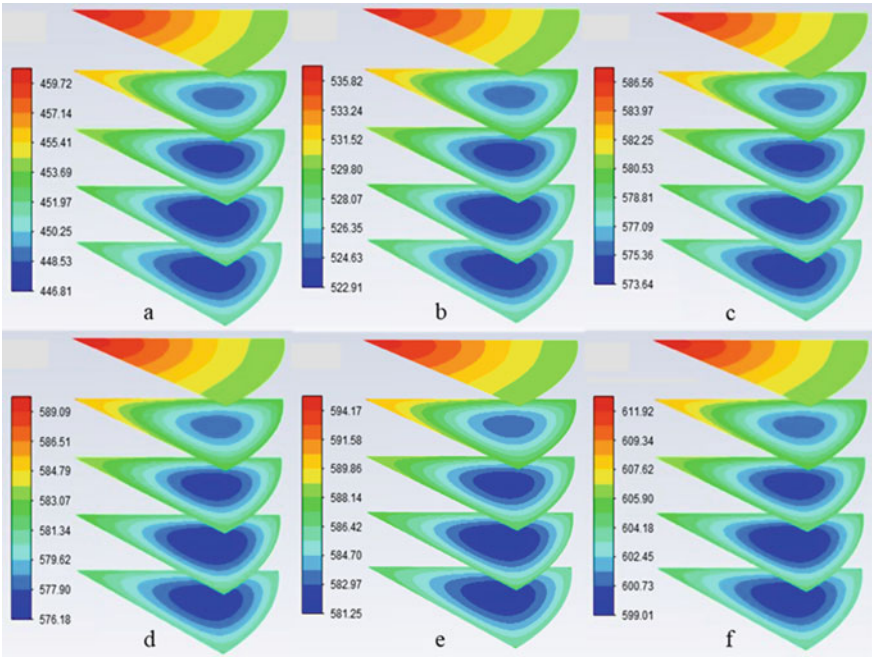

Fig. 23 Temperature (Kelvin) profile of PCM-CEG domain for 45° fin orientation at: **a** 6000 s, **b** 9000 s, **c** 11,000 s, **d** 11,100 s, **e** 11,300 s, and **f** 12,000 s

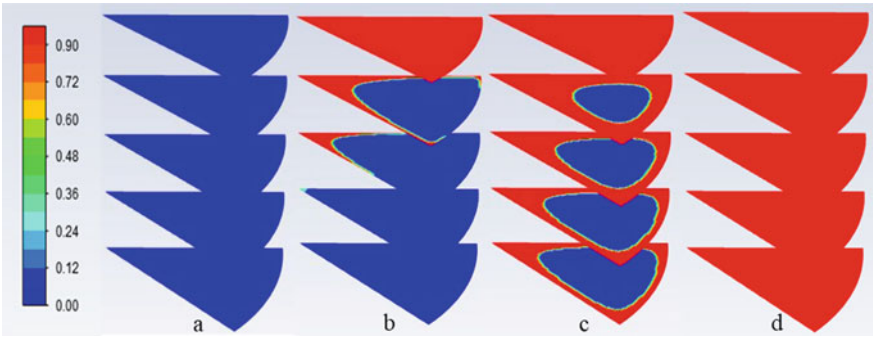

Fig. 24 Melting fraction profile in PCM-CEG domain in 45° fin orientation at: **a** 9000 s, **b** 11,000 s, **c** 11,100 s, and **d** 11,300 s

A close look at maximum temperatures obtained for these three orientations reveals another non-intuitive finding. Since 30° fin orientation offers more thermal uniformity, we expect the hotspot temperature to be the lowest for this configuration among the three chosen orientations. However, the temperature profiles given by Figs. 21f, 23f, and 25f predict the maximum temperatures in an exactly reverse

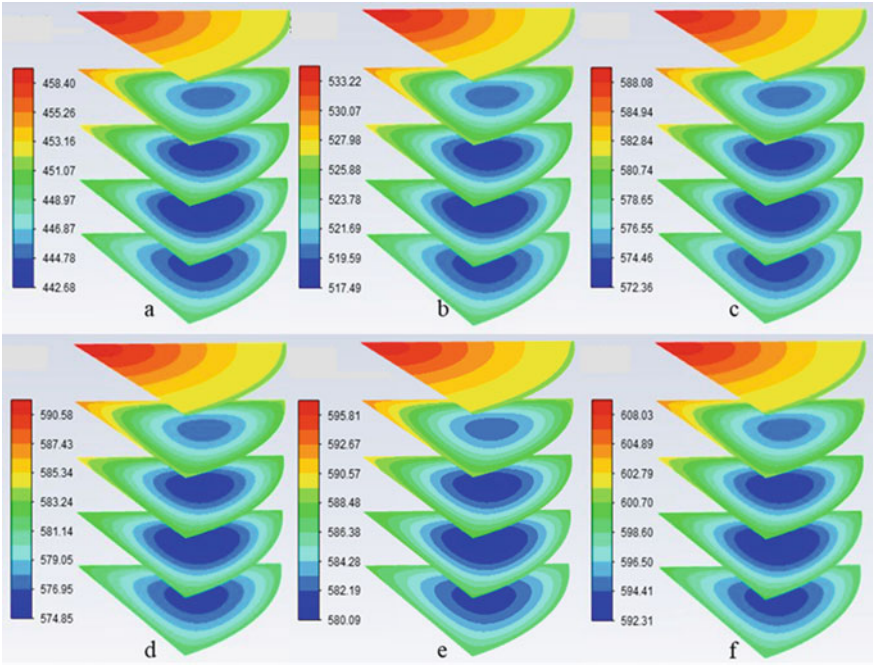

Fig. 25 Temperature (Kelvin) profile of PCM-CEG domain for 60° fin orientation at: **a** 6000 s, **b** 9000 s, **c** 11,200 s, **d** 11,300 s, **e** 11,510 s, and **f** 12,000 s

manner. The maximum temperature for 60° orientation is found to be the lowest (T_{max} = 335 °C), followed by 45° (T_{max} = 339 °C) and 30° (T_{max} = 345 °C) fin orientations. This reverse trend might be attributed to the loss of PCM-CEG volume due to the volume occupancy of the fines. The 30° fin orientation has maximum volume loss due to the presence of maximum number of fins. Equivalent energy pertaining to the latent heat storage potential of this lost volume of PCM must be accounted for and manifested by an equivalent rise in the sensible temperature of the entire storage unit. The excess maximum temperature is essentially the manifestation of the latent heat of fusion of the lost volume of PCM. However, in this context, a question may arise: why is the no-fin arrangement manifesting the lowest maximum temperature? The answer to this question can be comprehensively addressed by temperature larger non-uniformity of the no-fin arrangement. The absence of fins causes a much larger temperature gradient from the hotspot to lowest temperature region. Comparison of minimum temperatures between non-finned and finned orientations shows that the minimum temperature is lowest (∼303 °C) for no-fin configuration. We must remember that the total amount of heat supplied to all these orientations is the same. Therefore, larger non-uniformity of temperature leads to larger maximum temperature.

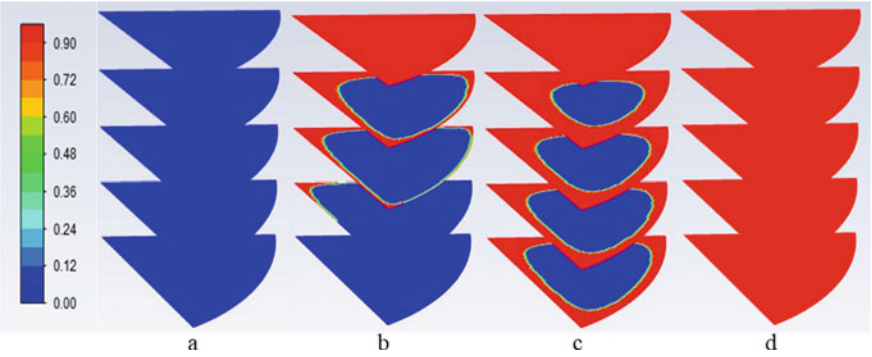

Fig. 26 Melting fraction profile in PCM-CEG domain for 60° fin orientation at: **a** 9000 s, **b** 11,200 s, **c** 11,300 s, and **d** 11,510 s

Next we compare the melt fraction evolution presented by Figs. 22, 24, and 26. Unlike no-fin configuration, the last region to melt is found to be the farthest region from the hotspot. As is evident, 30° fin orientation promotes fastest meltdown of the entire PCM with maximum temperature uniformity (minimum difference between $T_{\max}$ and $T_{\min}$). We observe another interesting fact corresponding to the onset and termination of melting process. The earliest onset of melting occurs for the no-fin configuration (Fig. 18). Large temperature non-uniformity leads to accumulation of heat in the hotspot region leading to an early rise in temperature above the melting point (T_m) in this region. However, the same large temperature non-uniformity causes the most delayed completion of melting process. For the finned configurations (Figs. 22, 24 and 26), the onset of melting gets delays as compared to no-fin configuration because the temperature uniformity causes the entire PCM-CEG domain to reach the melting point (T_m) uniformly deferring the hotspot temperature to reach T_m at an early stage. However, the complete melting duration is significantly smaller once onset of melting occurs.

In continuation to the discussion regarding the effect of fin arrangement on maximum temperature ($T_{\max}$) of the domain,, the time evolution of $T_{\max}$ and $T_{\min}$ is shown in Fig. 27 for different fin configurations. The case study involving no fin predicts maximum non-uniformity of the temperature field with $(T_{\max} - T_{\min}) \sim 70$ K. As the fin numbers are progressively increased (60°, 45°, and 30° fin orientations), $T_{\max} - T_{\min}$ values reduce subsequently indicating better uniformity of the thermal field. It is to be noted here, that the higher values of $T_{\max}$ associated with higher number of fins ($T_{\max\,@30^\circ} > T_{\max\,@45^\circ} > T_{\max\,@60^\circ}$) are also subjected to higher values of $T_{\min}$ evolution, i.e. $T_{\min\,@30^\circ} > T_{\min\,@45^\circ} > T_{\min\,@60^\circ}$, which is physically consistent.

Figure 28 shows the variation of overall melt fraction with respect to time. No-fin configuration promotes earliest onset of melting and most delayed completion of the same. The 30° fin configuration promotes next earliest onset of melting followed by the 45° and 60° fin configurations. The 30° fin configuration also has the steepest melt

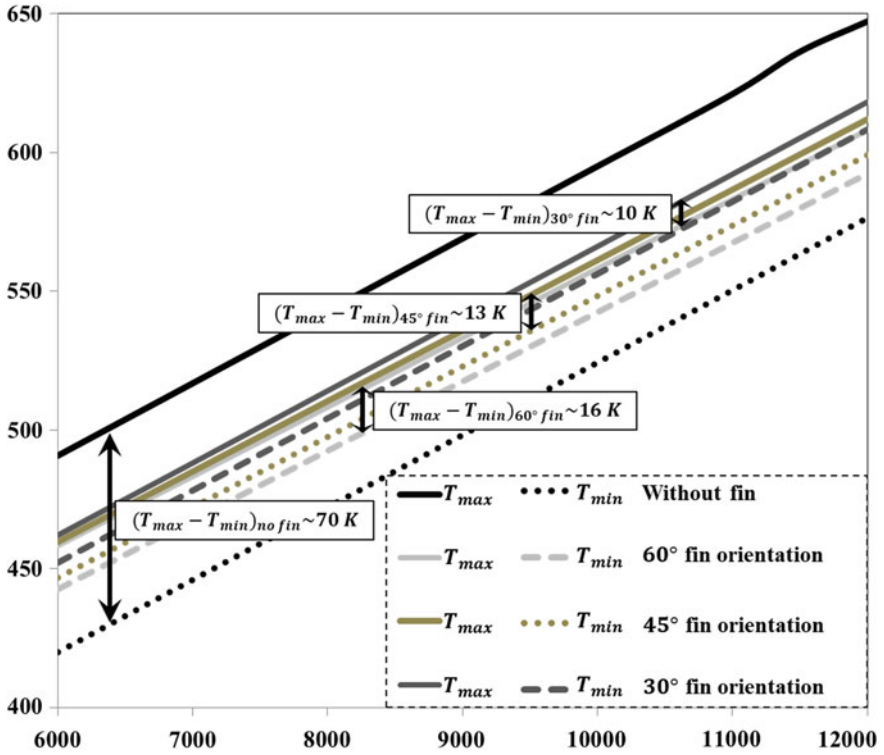

Fig. 27 Variation of maximum and minimum temperatures with time for different fin configurations; smaller difference between maximum and minimum temperature denotes more uniformity of temperature field

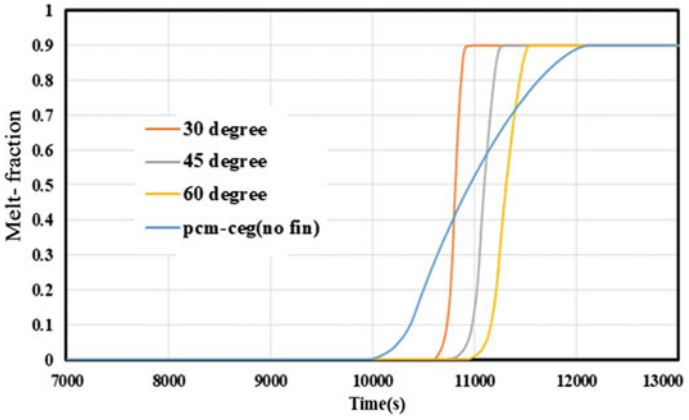

Fig. 28 Evolution of overall melt fraction with time

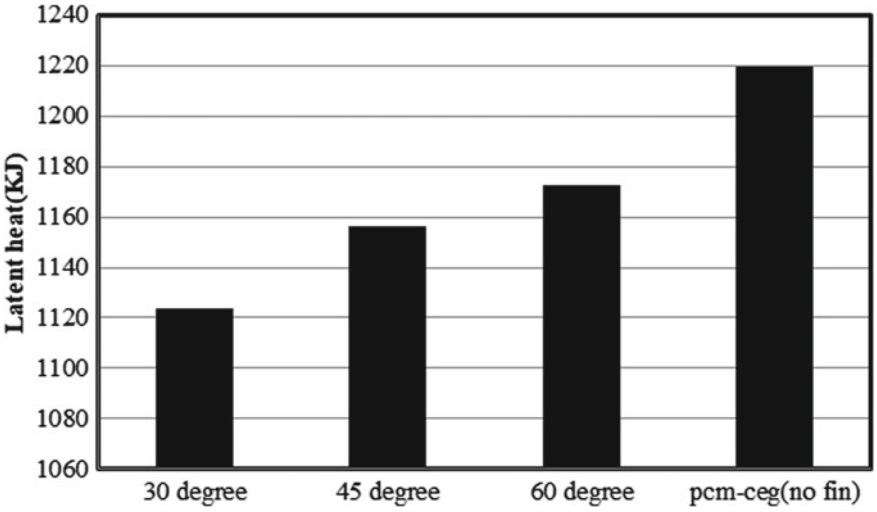

Fig. 29 Heat storage capacity (latent. heat) versus fin angle

fraction versus time plot, depicting fastest completion of melting process followed by 45° and 60° fin configurations.

Figure 29 shows latent heat storage capacity of four different configurations under consideration. Although increasing the total number of fins reduces the charging time significantly, the price we pay is the reduction in total latent heat capacity of the storage. Therefore, a tradeoff must be put into place to optimize between the charging duration and latent heat storage capacity.

5 Conclusion

An alternative design of parabolic dish solar cooker with double reflector arrangement integrated with latent heat storage unit located below the parabolic dish (primary reflector) is explored in terms of its thermal performance during the charging process. A diffusion dominated numerical model to address the melting of PCM in PCM-CEG composite is described. Effect of plate fins extended in radial direction and distributed circumferentially with prescribed angular pitch on the overall charging dynamics is studied. If fins are not incorporated, the maximum temperature (hotspot temperature) attained by the storage unit after completion of the charging process is found to be very close to the decomposition temperature of the PCM $NaNO_3$. Also, the temperature distribution in the storage medium is found to be highly non-uniform in the absence of fins. Addition of circumferentially distributed radial fins not only reduces the hotspot temperature to a safer margin, but it also establishes a much uniform thermal field within the storage medium. Three different fin orientations

are studied for angular pitch of 30°, 45°, and 60° with progressively lesser number of fins. Larger number of fins resulted in earlier attainment of complete melting. Although the onset of melting occurs at a much earlier time when fins are not added, the completion of melting can only be obtained after significantly large time duration due to large non-uniformity of the thermal field. On the other hand, addition of fins delays the onset of melting process, but once melting process starts completion of melting is attained at an incredibly short time span. When the maximum temperature evolution is compared for 30°, 45°, and 60° fin orientations, surprisingly higher values of maximum temperature is obtained for progressively higher number of fins ($T_{\max @30^\circ} > T_{\max @45^\circ} > T_{\max @60^\circ}$). However, the same trend is also observed when minimum temperatures are compared ($T_{\min @30^\circ} > T_{\min @45^\circ} > T_{\min @60^\circ}$) with the difference between maximum and minimum temperatures progressively reducing for higher number of fines ($[T_{\max} - T_{\mathrm{mean}}]_{@30^\circ} < [T_{\max} - T_{\mathrm{mean}}]_{@45^\circ} < [T_{\max} - T_{\mathrm{mean}}]_{@60^\circ}$) indicating attainment of better uniformity in the temperature field with larger number of fins, which is physically consistent.

References

Bennon WD, Incropera FP (1987) A continuum model for momentum, heat and species transport in binary solid-liquid phase change systems—I. Model formulation. Int J Heat Mass Transf 30(10):2161–2170

Bhave AG, Thakare KA (2018) Development of a solar thermal storage cum cooking device using salt hydrate. Sol Energy 171:784–789

Bodzenta J, Mazur J, Kaźmierczak-Bałata A (2011) Thermal properties of compressed expanded graphite: photothermal measurements. Appl Phys B 105(3):623–630

Brent AD, Voller VR, Reid KJ (1988) The enthalpy porosity technique for modelling convection diffusion phase change: application to the melting of a pure metal. Numer Heat Transf 13:297–318

Buddhi D, Sahoo LK (1997) Solar cooker with latent heat storage: design and experimental testing. Energy Convers Manag 38(5):493–498

Buddhi D, Sharma SD, Sharma A (2003) Thermal performance evaluation of a latent heat storage unit for late evening cooking in a solar cooker having three reflectors. Energy Convers Manag 44(6):809–817

Chakraborty PR (2017) Enthalpy porosity model for melting and solidification of pure substances with large difference in phase specific heats. Inte Commun Heat Mass Transf 81:183–189

Coccia G, Di Nicola G, Tomassetti S, Pierantozzi M, Chieruzzi M, Torre L (2018) Experimental validation of a high-temperature solar box cooker with a solar-salt-based thermal storage unit. Sol Energy 170:1016–1025

Cuce PM (2018) Box type solar cookers with sensible thermal energy storage medium: a comparative experimental investigation and thermodynamic analysis. Sol Energy 166:432–440

Domanski R, El-Sebaii AA, Jaworski M (1995) Cooking during off-sunshine hours using PCMs as storage media. Energy 20(7):607–616

El-Sebaii AA, Al-Amir S, Al-Marzouki FM, Faidah AS, Al-Ghamdi A, Al-Heniti S (2009) Fast thermal cycling of acetanilide and magnesium chloride hexahydrate for indoor solar cooking. Energy Convers Manag 50(12):3104–3111

Fluent ANSYS (2015) Ansys fluent. Academic Research. Release, 14

Foong CW, Hustad JE, Løvseth J, Nydal OJ (2010) Numerical study of a high temperature latent heat storage (200–300 °C) using eutectic nitrate salt of sodium nitrate and potassium nitrate. In: Proceedings of the COMSOL conference

Horne S (2012) Concentrating photovoltaic (CPV) systems and applications. In: Concentrating solar power technology. Woodhead Publishing, pp 323–361
https://www.nrel.gov/gis/data_solar.html
Hussein HMS, El-Ghetany HH, Nada SA (2008) Experimental investigation of novel indirect solar cooker with indoor PCM thermal storage and cooking unit. Energy Convers Manage 49(8):2237–2246
Iverson BD, Broome ST, Kruizenga AM, Cordaro JG (2012) Thermal and mechanical properties of nitrate thermal storage salts in the solid-phase. Sol Energy 86(10):2897–2911
Kalnæs SE, Jelle BP (2015) Phase change materials and products for building applications: a state-of-the-art review and future research opportunities. Energy Build 94:150–176
Kenisarin MM (2010) High-temperature phase change materials for thermal energy storage. Renew Sustain Energy Rev 14(3):955–970
Kumaresan G, Raju G, Iniyan S, Velraj R (2015) CFD analysis of flow and geometric parameter for a double walled solar cooking unit. Appl Math Model 39(1):137–146
Kumaresan G, Vigneswaran VS, Esakkimuthu S, Velraj R (2016) Performance assessment of a solar domestic cooking unit integrated with thermal energy storage system. J Energy Storage 6:70–79
Lecuona A, Nogueira JI, Ventas R, Legrand M (2013) Solar cooker of the portable parabolic type incorporating heat storage based on PCM. Appl Energy 111:1136–1146
Mallow A, Abdelaziz O, Graham S Jr (2016) Thermal charging study of compressed expanded natural graphite/phase change material composites. Carbon 109:495–504
Memon SA (2014) Phase change materials integrated in building walls: a state of the art review. Renew Sustain Energy Rev 31:870–906
Moreno P, Miró L, Solé A, Barreneche C, Solé C, Martorell I, Cabeza LF (2014) Corrosion of metal and metal alloy containers in contact with phase change materials (PCM) for potential heating and cooling applications. Appl Energy 125:238–245
Mukherjee D (2018) A review study on the thermo physical properties and storage applications of phase change materials. World Sci News 98:185–198
Patankar S (2018) Numerical heat transfer and fluid flow. CRC Press
Py X, Olives R, Mauran S (2001) Paraffin/porous-graphite-matrix composite as a high and constant power thermal storage material. Int J Heat Mass Transf 44(14):2727–2737
Sarbu I, Dorca A (2019) Review on heat transfer analysis in thermal energy storage using latent heat storage systems and phase change materials. Int J Energy Res 43(1):29–64
Sharma SD, Iwata T, Kitano H, Sagara K (2005) Thermal performance of a solar cooker based on an evacuated tube solar collector with a PCM storage unit. Sol Energy 78(3):416–426
Sharma A, Tyagi VV, Chen CR, Buddhi D (2009) Review on thermal energy storage with phase change materials and applica-tions. Renew Sustain Energy Rev 13(2):318–345
Shrivastava A, Chakraborty PR (2019) Shell-and-tube latent heat thermal energy storage (ST-LHTES). In: Advances in solar energy research. Springer, Singapore, pp 395-441
Venkateshwar K, Mathur V, Chakraborty PR (2017) Feasibility of using phase change material for thermal storage at high temperature for concentrated solar cooker: a numerical approach. In: Proceeding of SEEC2017-121
Veremachi A, Cuamba BC, Zia A, Lovseth J, Nydal OJ (2016) PCM heat storage charged with a double-reflector solar system. J Solar Energy 2016
Vigneswaran VS, Kumaresan G, Sudhakar P, Santosh R (2017) Performance evaluation of solar box cooker assisted with latent heat energy storage system for cooking application. In: IOP conference series: earth and environmental science, vol 67, no 1, p 012017. IOP Publishing
Zalba B, Marın JM, Cabeza LF, Mehling H (2003) Review on thermal energy storage with phase change: materials, heat transfer analysis and applications. Appl Therm Eng 23(3):251–283